Supporting Information

Alloying Pd with Ru enables electroreduction of nitrate to ammonia with ~100% Faradaic efficiency over a wide potential window

Yue Hu[a,b], Jiawei Liu[c], Wenyu Luo[b], Jinfeng Dong[b], Carmen Lee[b], Nan Zhang[d], Mengxin Chen[b], Yifan Xu[b], Dongshuang Wu[b], Mingsheng Zhang[c], Qiang Zhu[c], Erhai Hu[b], Dongsheng Geng[e,]*, Lixiang Zhong[f,]*, and Qingyu Yan[b,c,]*

[a]*School of Mathematics and Physics, University of Science and Technology Beijing, Beijing 100083, China*

[b]*School of Materials Science and Engineering, Nanyang Technological University, 639798 Singapore*

[c]*Institute of Materials Research and Engineering, A*STAR, 138634 Singapore*

[d]*State Key Laboratory of Applied Organic Chemistry, Frontiers Science Center for Rare Isotopes, College of Chemistry and Chemical Engineering, Lanzhou University, Lanzhou 730000, China*

[e]*School of Chemistry and Materials Science, Nanjing University of Information Science & Technology, Nanjing 210044, China*

[f]*School of Physics, Beijing Institute of Technology, Beijing, 100081, China*

*Corresponding author: dgeng@nuist.edu.cn

zhonglx@bit.edu.cn

AlexYan@ntu.edu.sg

Methods

Chemicals

All the chemicals are at analytical grade and used without further purification. Nitric acid (HNO_3, 69%) was purchased from Honeywell. Sodium hydroxide (NaOH, 99%) was purchased from Schedelco. Palladium chloride ($PdCl_2$, ≥99.9%), Ruthenium(III) chloride trihydrate ($RuCl_3 \cdot 3H_2O$, ≥99.9%), potassium bicarbonate ($KHCO_3$, 99.7%), hydrochloric acid (HCl, 37%), potassium hydroxide (KOH, 90%), potassium nitrate (KNO_3, ≥99%), potassium nitrate-^{15}N ($K^{15}NO_3$, ≥99%), nitrite Standard for IC (1000 mg/L nitrite in water), ammonium chloride (NH_4Cl, ≥99.5%), salicylic acid ($C_7H_6O_3$, ≥99%), sodium citrate tribasic dihydrate ($C_6H_5Na_3O_7 \cdot 2H_2O$, ≥99%), sodium hypochlorite solution (NaClO, available chlorine 4.00-4.99%), sodium nitroferricyanide dihydrate ($C_5FeN_6Na_2O \cdot 2H_2O$, ≥99%), deuterium oxide (D_2O, 99.95%), dimethyl sulfoxide (DMSO, $(CH_3)_2SO$, ≥99.9%), and Nafion™ 117 containing solution (~5% in a mixture of lower aliphatic alcohols and water) were purchased from Sigma-Aldrich. Hydrophilic carbon fiber paper (CFP, TGP-H-090) was purchased from Tianjin Annuohe New Energy Technology Co., Ltd. Nafion 117 membrane was purchased from The Fuel Cell Store. Deionized (DI) water of 18.2 MΩ·cm was used in all the experiments.

Preparation of Pd_xRu_y, Pd and Ru nanocrystals (NCs)

Pd_xRu_y NCs were prepared via a co-electrodeposition process under galvanostatic current density of 20 mA cm^{-2} for 20 min in a three-electrodes system, where a saturated calomel electrode, a platinum plate, and a 1×2 cm^2 hydrophilic CFP were used as the reference, counter, and working electrodes, respectively. CFP was sequentially ultrasonically pretreated in acetone, and ethanol, and then repeatedly rinsed with DI water. The deposition electrolyte (40 ml) consisted of 30 ml saturated 0.1 M $KHCO_3$ solution and 10 ml catalyst precursor solution. Among them, the catalyst precursor solution was composed of $PdCl_2$ and $RuCl_3 \cdot 3H_2O$ with different Pd/Ru molar ratios (9:1, 3:1, and 1:1), with the total metal ions of 0.2 mM. The solution was made transparent with HCl (37%) and brought to 10 ml with DI water. During the electroreduction process, CO_2 was continuously bubbled at a rate of 20 sccm. After the electrodeposition process, the obtained Pd_xRu_y NCs on CFP was rinsed repeatedly with DI water, and then dried at 60°C in a vacuum oven. The preparation of monometallic Pd and Ru NCs follows the same steps as the synthesis of Pd_xRu_y NCs, except that a single component of 0.2 mM $PdCl_2$ or $RuCl_3 \cdot 3H_2O$ was used in the catalyst precursor solution, respectively. By weighing the CFPs before and after electrodeposition, the loadings of Pd_xRu_y NCs, Pd, and Ru

deposited onto the CFPs were all about 1.6 mg cm^{-2}.

Catalyst Characterizations

The samples were confirmed by X-ray diffraction (XRD) using the Bruker D8 X-ray diffractometer with Cu Kα radiation (λ = 0.15406 nm). The structure and elemental composition were characterized by transmission electron microscopy (TEM), high-resolution TEM (HRTEM), high-angle annular dark-field scanning transmission electron microscopy (HAADF-STEM), and energy-dispersive spectroscopy (EDS) elemental mapping using a JEOL 2100F microscope at an accelerating voltage of 200 kV. The chemical composition was analyzed by X-ray photoelectron spectroscopy (XPS) using a Kratos AXIS Supra+ x-ray photoelectron spectroscopy. X-ray absorption fine spectroscopy (XAFS) experiments of the Ru K-edge and Pd K-edge were performed using a Si (311) monochromator crystal at the BL14B2 beamline at SPring-8, in Japan. The operando Fourier transform infrared spectroscopy (FTIR) tests were carried out jointly by the BRUKER-Fourier Transform Infrared Spectrometer-TENSOR27 and a CHI-760E electrochemical workstation using a customized cell, with a saturated Hg/HgO reference electrode and a Pt ring counter electrode in 1 M KOH.

Electrochemical tests

The electrochemical tests were performed using a typical three-electrodes system connected to the Solartron electrochemical workstation (England) in H-type cell. The Pd_xRu_y/CFPs, Hg/HgO electrode (filled with 1 M KOH aqueous solution) and platinum plate were used as working, reference and counter electrodes, respectively. The H-type cell was separated by Nafion 117 membrane, which was pretreated with H_2O_2 (2%) and H_2SO_4 (0.5 M) at 80℃ for 1 h, respectively. For the tests of eNO_3^- RR, 1 M KOH aqueous solution (PH=14, determined by a Seven2Go pH Meter, Switzerland) was used as an electrolyte, with 50 ml each in the cathode and anode compartments. Different concentrations of KNO_3 were added into the cathode compartment for eNO_3^-RR. During the operation, Ar was continuously bubbled into the electrolyte in cathode compartment to shield the air interference, and the magnetic stirring was continued at a speed of 650 rpm. All potentials measured were referenced against reversible hydrogen electrode (RHE) by $E_{(V\ vs.\ RHE)} = E_{(V\ vs.\ Hg/HgO)} + 0.0591 \times PH + 0.098$. Note that the change in pH of the electrolyte during the reaction is negligible. The current density was normalized to the geometric electrode area (1 cm^2) and the potential was not iR compensated, unless otherwise specified. Before all formal testing, 50 cyclic voltammetry (CV) cycles (in the potential range of 0.3 to -0.7 V with a scan rate of

50 mV s^{-1}) were performed in 1 M KOH aqueous solution to allow sufficient structural evolution of the catalysts to a steady state. The electrochemically active surface area (ECSA) was evaluated by a double-layer capacitance method. The CV scans were conducted over a potential range of 0.53 to 0.55 V where no Faradaic current occurred, at different scan rates of 2, 4, 6, 8, and 10 mV s^{-1}. Linear sweep voltammetry (LSV) was performed with a scanning rate of 5 mV s^{-1}. Electrochemical impedance spectroscopy was measured at frequencies from 0.01 Hz to 100 kHz using an Autolab potentiostat (M204) under the applied potential of -0.2 V.

Kinetic evaluation

The electrochemical kinetic analysis of eNO_3^-RR was performed according to the Koutecký–Levich (K–L) equation:[1]

$$\frac{1}{i_m} = \frac{1}{i_k} + \frac{1}{0.2nFD^{2/3}v^{-1/6}C\omega^{1/2}}$$

Where i_m is the measured current density, mA cm^{-2}; i_k is the kinetic current of eNO_3^-RR; n is the number of electrons transferred in the reaction; F is the Faraday constant of 96485.3383 C mol^{-1}; D represents the effective diffusion coefficient of 0.1 M NO_3^- at 25℃, 1.4×10^{-5} cm^2s^{-1}; v represents the kinematic viscosity of water at 25℃, 1×10^{-2} cm^2 s^{-1}; C is the concentration of NO_3^-, mol L^{-1}; ω is the electrode rotation speed, rpm.

An Autolab rotating electrode (RDE) with a diameter of 0.3 cm deposited with 5 μL of the prepared homogeneous catalyst ink was used as the working electrode. The homogeneous catalyst ink was prepared as 10 mg of the catalyst powder scraped off from Pd_xRu_y/CFPs was dispersed in 1 mL of ethanol solution containing 120 μL of Nafion 117 solution, followed by sonication of the mixed solution for 1 h. LSV measurements were performed in 1 M KOH aqueous solution (50 ml) with 0.1 M KNO_3 at different rotation speeds (400, 625, 900 and 1600 rpm) with a scan rate of 5 mV s^{-1}. Ar was continuously bubbled into the electrolyte to remove dissolved O_2 and N_2.

Determination of N-containning species

Determination of NH_3. As-produced NH_3 was spectrophotometrically determined by the indophenol blue method with modification.[2] First, a certain amount of post-reaction electrolyte was collected and diluted to the detection range of NH_3 with 1 M KOH, and took 2 ml of the diluted electrolyte into an 8 ml glass vial. Then 2 ml of 1 M NaOH solution containing 5 wt% $C_5FeN_6Na_2O\cdot2H_2O$ and 5 wt% $C_6H_5Na_3O_7\cdot2H_2O$ was added, followed by addition of 1 ml of 0.05 M NaClO solution and 0.2 ml of 1 wt% $C_5FeN_6Na_2O\cdot2H_2O$ aqueous solution. After keeping at room temperature for 2 h for the

sufficient colour reaction, the absorption spectrum of the resulting solution was measured using an UV–vis spectrophotometer (Shimadzu UV-2700i). The absorbance at ~655 nm was used to determine the concentration of NH_3. The concentration−absorbance curve was calibrated using a series of standard NH_4Cl solutions (0, 0.5, 1.0, 2.0, 3.0, 4.0 and 5.0 μg ml^{-1}) in 1 M KOH electrolyte.

Determination of NO_2^-. The produced NO_2^- was quantified by ion chromatogram instrument (930 compact IC Flex, Metrohm). Different concentrations of nitrite Standard solution for IC (0, 0.1, 0.2, 0.4, 0.6, 0.8, and 1.0 μg ml^{-1}) were used to build the area-concentration calibration curve of NO_2^-. A certain amount of post-reaction electrolyte was collected and diluted 100 times with deionized water, and took 12 ml of the diluted electrolyte for detection.

Determination of NO_3^-. Reactant NO_3^- was also quantified by ion chromatogram instrument. The calibration curve was built using a series of standard KNO_3 solutions (0, 0.01, 0.05, 0.10, 0.15, 0.20, 0.25, and 0.30 mM). The detection process was consistent with that of NO_2^-.

N isotope labelling experiments

The ^1H magnetic resonance (NMR) spectroscopy was collected on a Bruker Avance III HD 800 MHz (18.8 T) standard-bore NMR spectrometer. Specifically, the collected post-reaction electrolyte was first diluted to the detection range of NH_3 and the PH was adjusted to 2 with HCl. Next, 0.4 ml of the sample solution was mixed with 0.1 ml of D_2O and 0.1 ml of DMSO aqueous solution (10 ppm) in an NMR tube (Ø, 5 mm), where DMSO serves as internal standard. The test was conducted with water suppression by using the pre-saturation technique.

^1H NMR spectroscopy was also used to quantify the $^{15}NH_4^+$ yield rate after eNO_3^-RR in 1 M KOH with different $^{15}NO_3^-$ concentrations at -0.3 V. The calibration curves with defined $^{15}NH_4Cl$ concentrations were constructed as standards. Specifically, (1) a series of $^{15}NH_4Cl$ solutions with known concentrations (0.5, 1, 2.5, 5, 10 mM) were prepared in 1 M NaOH as standards; (2) The standard solutions were adjust to pH 2.0 by adding HCl; (3) 30 mL of the above standard solutions were mixed with 0.012 g maleic acid; (4) 50 μL of D_2O was added in 0.5 mL above mixed solutions for the NMR detection.

Calculation of average NH_3 FE (FE_{NH_3}) and NO_2^- FE ($FE_{NO_2^-}$), NH_3 yield rate (Y_{NH_3}) and NH_3 partial current density (j_{NH_3})

The average FE_{NH_3} was calculated as follows:

$$FE_{NH_3} = \frac{8F \times C_{NH_3} \times V}{Q}$$

Where C_{NH_3} is the detected concentration of NH_3 (M), V is the volume of the electrolyte (0.05 L), and Q is the total charge passed through the working electrode (C).

The average $FE_{NO_2^-}$ was calculated as follows:

$$FE_{NO_2^-} = \frac{2F \times C_{NO_2^-} \times V}{Q}$$

Where $C_{NO_2^-}$ is the detected concentration of NO_2^- (M).

The average NH_3 yield rate was calculated as follows:

$$Y_{NH_3} = \frac{C_{NH_3} \times V}{A \times t}$$

Where A is the electrode geometric area, and t is the electrolysis time (h).

The j_{NH_3} was calculated as follows:

$$j_{NH_3} = \frac{Q \times FE_{NH_3}}{A \times t}$$

Density functional theory (DFT) calculations

All the calculations were performed using density functional theory (DFT) as implemented in the Vienna ab initio simulation package (VASP).[3, 4] The ion-electron interactions were treated with the projected augmented wave (PAW) pseudopotentials,[5] and the plane-wave basis set was cut off at 400 eV. The general gradient approximation (GGA) parameterized by Perdew, Burke, and Ernzerhof (PBE) was used to describe the exchange-correlation.[6] All structures were fully relaxed by the conjugate gradient method until the force component on each unfixed atom was less than 0.01 eV/Å, and the convergence criterion of total energy in the self-consistent field method was set to 10^{-5} eV. Closed-packed Pd(111), Ru(0001), and Pd_3Ru(111) slab models with four layers of atoms were used in our simulations to represent the dominant surfaces of Pd, Ru, and $Pd_{74}Ru_{26}$ nanocrystals, respectively. The bottom two layers of atoms in the slab models were fixed during structure relaxations. The optimized lattice constants are a = b = c = 3.936 Å, α = β = γ = 90° for Pd; a = b = 2.717 Å, c = 4.292 Å, α = β =90°, γ = 120° for Ru; and a = b = c = 3.898 Å, α = β = γ = 90° for Pd_3Ru. The thickness of vacuum in the slab models is larger than 15 Å to make sure that there is no superficial interaction between different slabs. The sizes of slab supercells are larger than 10 Å, and the k-point grid used for the Brillouin-zone integration was 3×3×1 sampled by the Monkhorst-Pack scheme.[7] The

adsorption free energies of reaction intermediates were calculated by using the computational hydrogen electrode (CHE) model developed by Nørskov et al.[8]

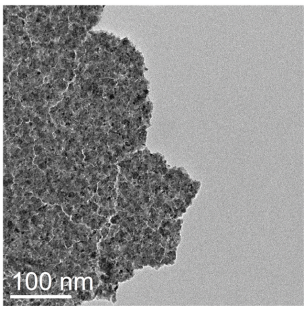

Figure S1. TEM image of PdRu NCs synthesized by the co-electrodeposition of Pd and Ru (the ratio of precursor Pd and Ru ions is 3:1) without CO_2 assistance.

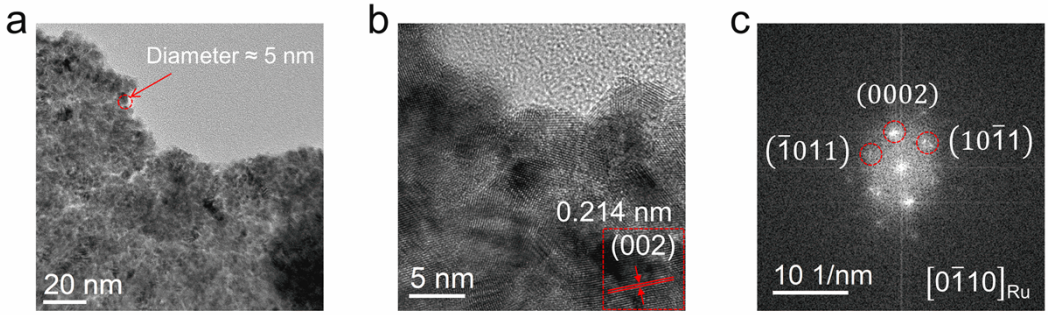

Figure S2. Structure characterization of Ru NCs. (a) TEM image. (b) HRTEM image. (c) The corresponding fast Fourier-transform (FFT) pattern of the selected area with the red dashed square in (b).

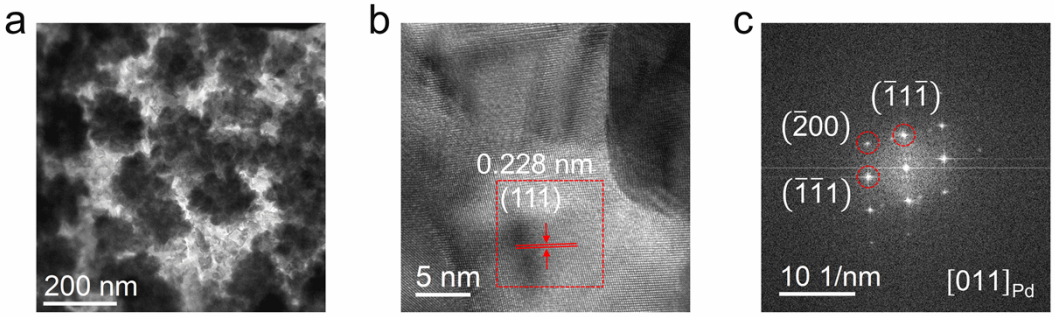

Figure S3. Structure characterization of Pd NCs. (a) TEM image. (b) HRTEM image. (c) The corresponding fast Fourier-transform (FFT) pattern of the selected area with the red dashed square in (b).

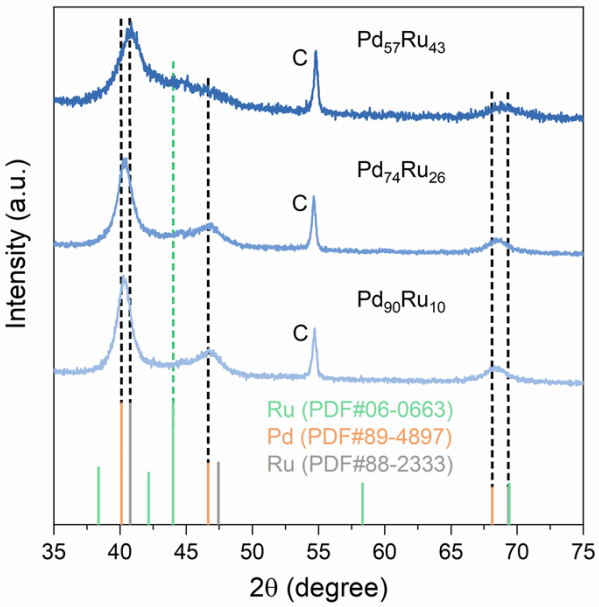

Figure S4. XRD patterns of $Pd_{90}Ru_{10}$, $Pd_{74}Ru_{26}$ and $Pd_{57}Ru_{43}$ NCs.

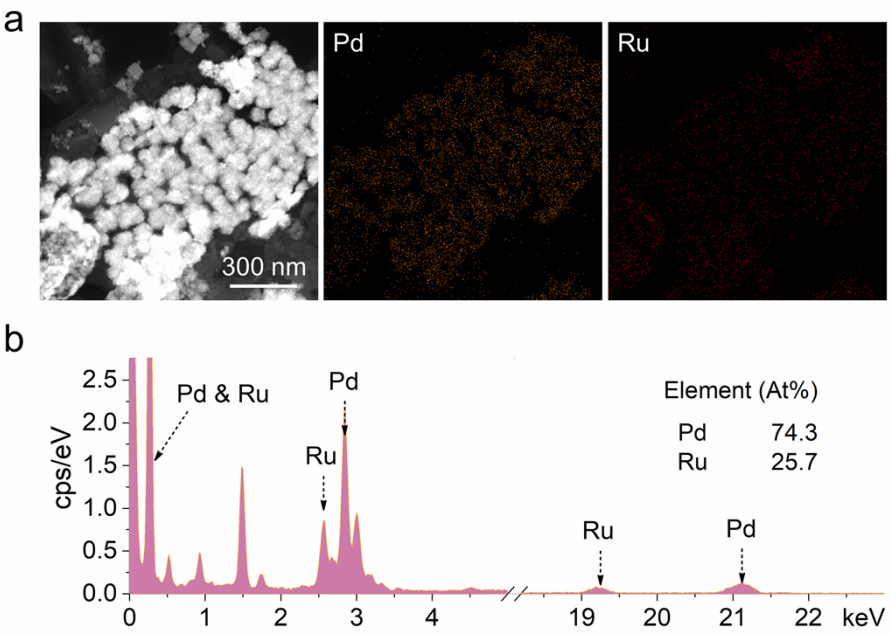

Figure S5. (a) EDS elemental mapping images of $Pd_{74}Ru_{26}$ NCs. (b) The corresponding EDS spectrum with the calculated atomic ratio of Pd and Ru.

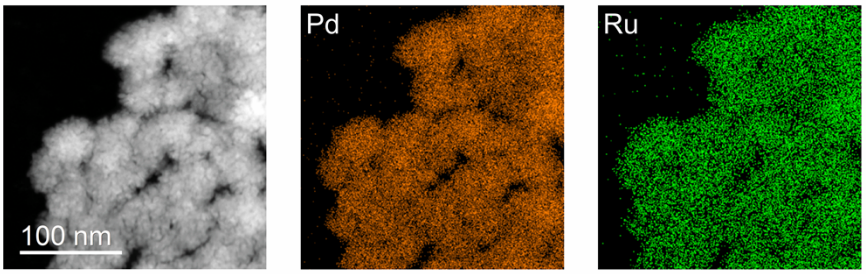

Figure S6. (a) Scanning TEM image of $Pd_{90}Ru_{10}$ NCs and the corresponding EDS elemental mapping images.

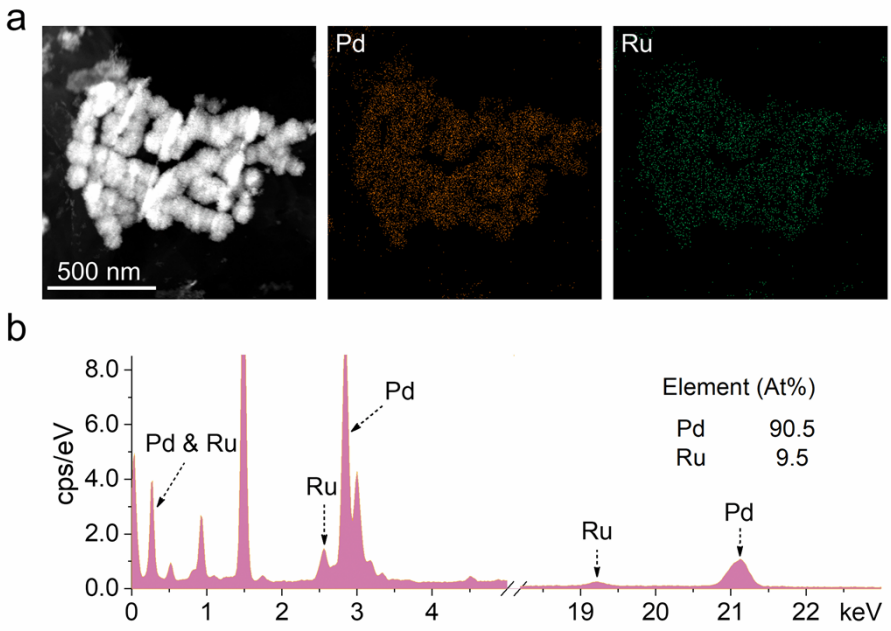

Figure S7. (a) EDS elemental mapping images of $Pd_{90}Ru_{10}$ NCs. (b) The corresponding EDS spectrum with the calculated atomic ratio of Pd and Ru.

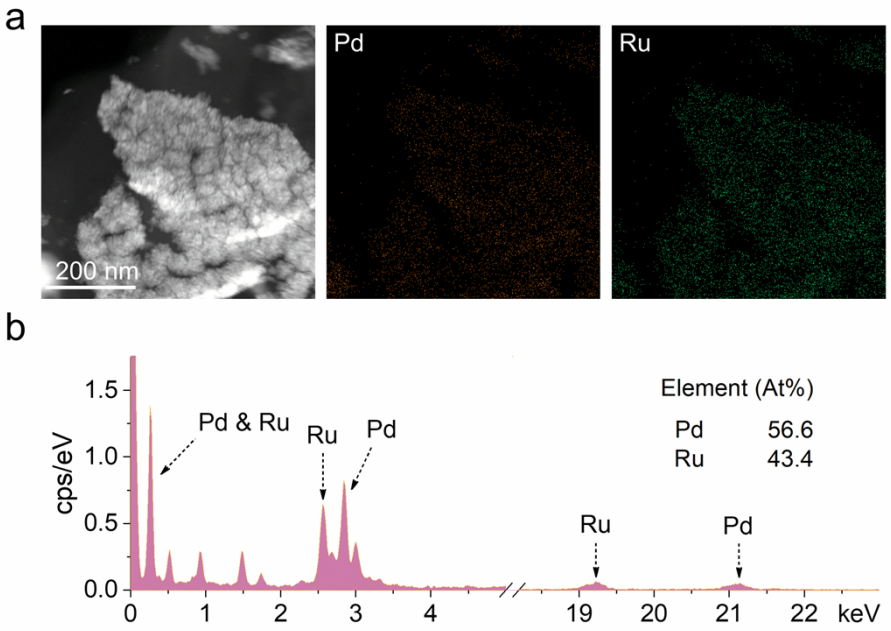

Figure S8. (a) EDS elemental mapping images of $Pd_{57}Ru_{43}$ NCs. (b) The corresponding EDS spectrum with the calculated atomic ratio of Pd and Ru.

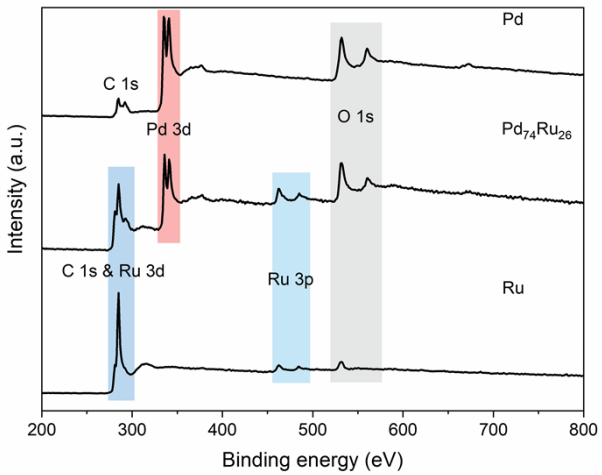

Figure S9. XPS survey spectra of Pd, $Pd_{74}Ru_{26}$ and Ru NCs.

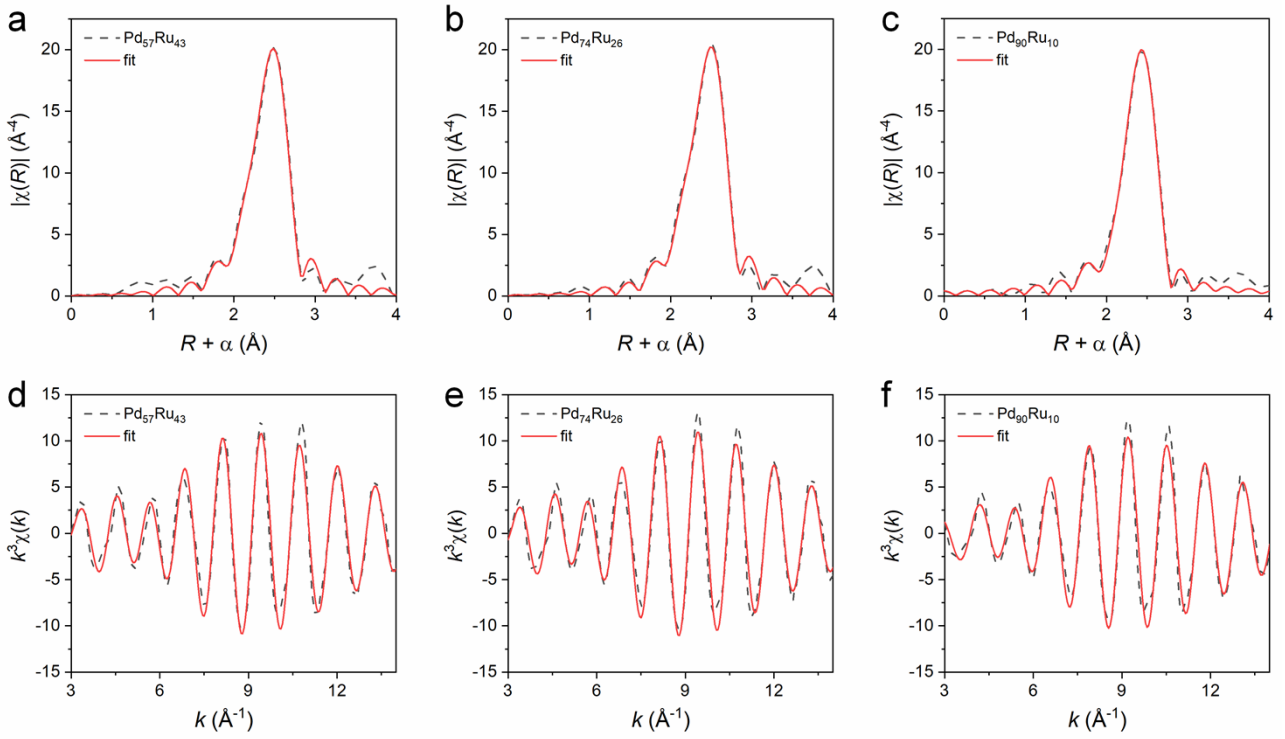

Figure S10. Pd K-edge EXAFS spectra in R space and fitting for $Pd_{57}Ru_{43}$ (a), $Pd_{74}Ru_{26}$ (b), and $Pd_{90}Ru_{10}$ (c), as well as EXAFS oscillation functions and fitting at the Pd K-edge of $Pd_{57}Ru_{43}$ (d), $Pd_{74}Ru_{26}$ (e), and $Pd_{90}Ru_{10}$ (f).

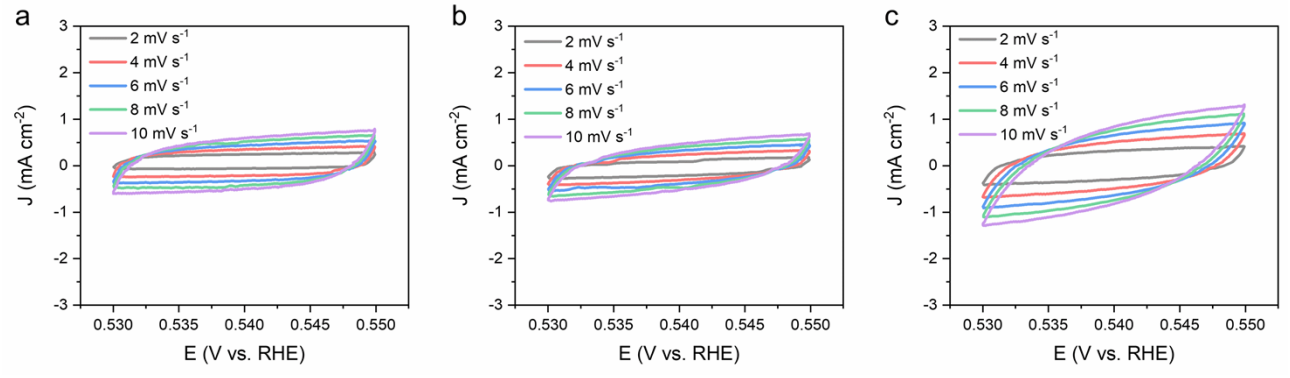

Figure S11. CV curves obtained on the Pd NCs (a), Ru NCs (b), and $Pd_{74}Ru_{26}$ NCs (c) at the scan rate of 2, 4, 6, 8 and 10 mV s^{-1}, respectively.

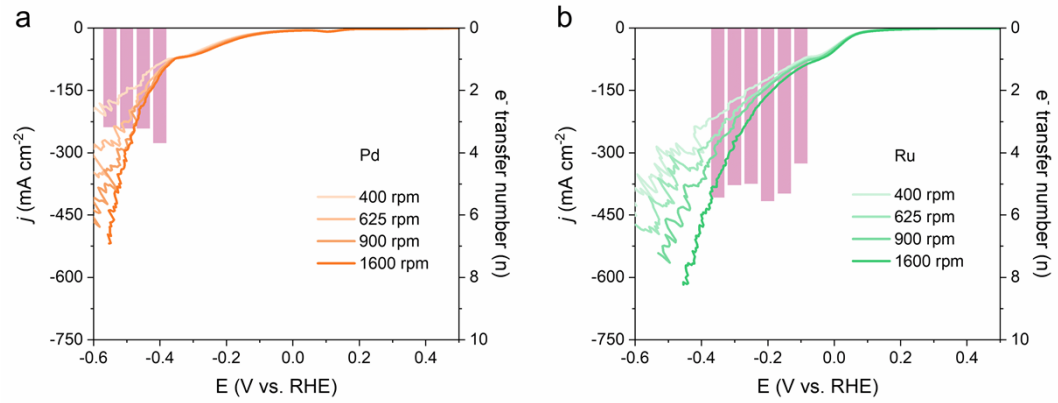

Figure S12. LSV curves (80% iR corrected) at different rotation rates and corresponding electron transfer numbers at different potentials for Pd (a) and Ru (b) on RDE in 1 M KOH with 0.1 M NO_3^-.

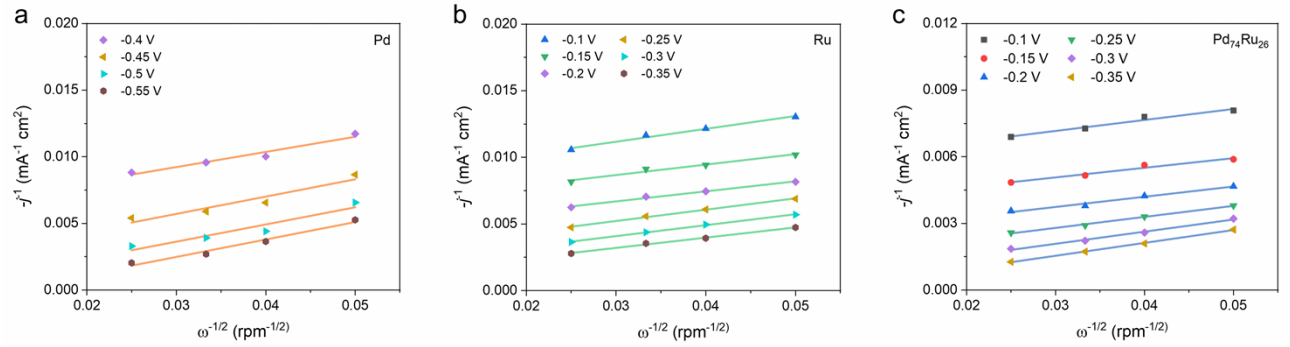

Figure S13. Koutecký-Levich plots of different potentials on Pd (a), Ru (b) and $Pd_{74}Ru_{26}$ (c).

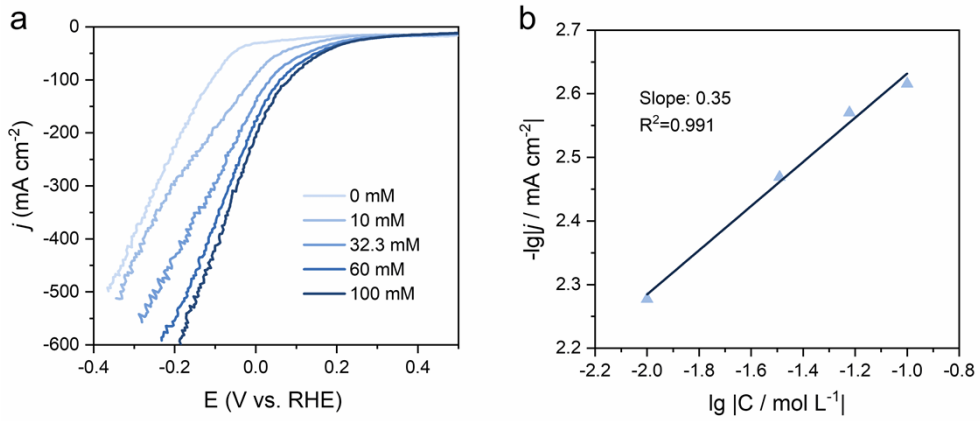

Figure S14. LSV curves (80% iR corrected) of $Pd_{74}Ru_{26}$ at 1 M KOH with different NO_3^- concentrations (a), and the corresponding lg(-*j*)-lg(C) plots fitted at 0.1 V (b).

A quasi-first-order reaction kinetics relationship between current density and NO_3^- concentrations on $Pd_{74}Ru_{26}$ at -0.1 V is obtained. This indicates that eNO_3^-RR on $Pd_{74}Ru_{26}$ driven by this potential is only related to the adsorption of NO_3^-. It is only limited by the mass transfer rate of NO_3^- to the catalytic site caused by the concentration difference, and is not subject to the kinetic constraints of the intermediate reaction steps. This is because the adsorbed NO_3^- on the catalytic site can quickly undergo a direct 8-electron transfer reaction and be converted into NH_3, as analyzed for the Koutecký-Levich plots.

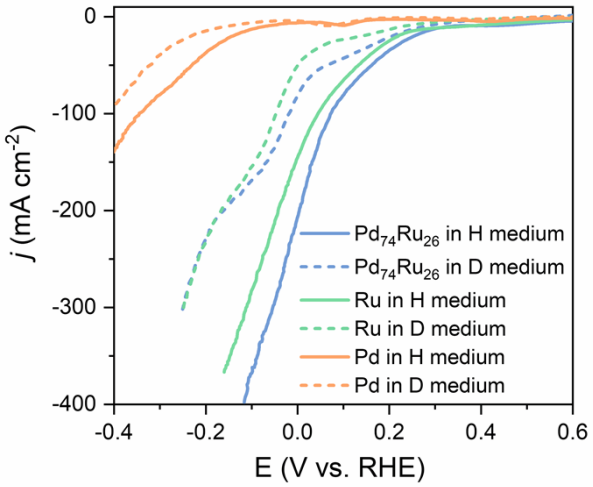

Figure S15. LSV curves of Pd, Ru and $Pd_{74}Ru_{26}$ NCs in a purely protic medium (1 M NaOH+H_2O+0.1 M KNO_3^-) and a purely deuterium medium (1 M NaOD+D_2O+0.1 M KNO_3^-).

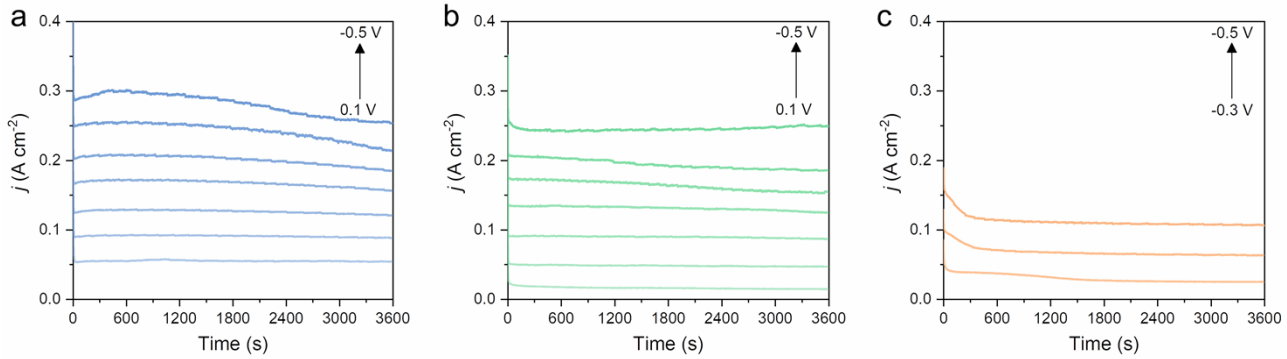

Figure S16. The i-t curves of Pd (a) at applied potentials from -0.3 to -0.5 V, Ru (b) at applied potentials from 0.1 to -0.5 V, and $Pd_{74}Ru_{26}$ (c) at applied potentials from 0.1 to -0.5 V in 1 M KOH with 32.3 mM NO_3^-.

The i-t curves show that $Pd_{74}Ru_{26}$ consistently exhibits higher current density than Ru and Pd at each applied potential, indicating its superior eNO_3^-RR activity. The current density of $Pd_{74}Ru_{26}$ decreased over time at relatively high potentials of -0.4 and -0.5 V, which is due to the gradual consumption of NO_3^- in the electrolyte. This is also an indication of the good electrochemical response of $Pd_{74}Ru_{26}$ to NO_3^-.

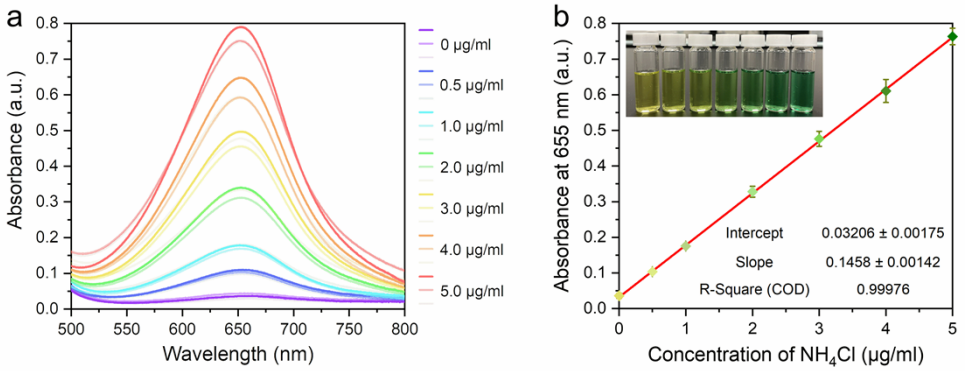

Figure S17. (a) Absorbance UV-vis spectra of standard NH_4Cl with different concentrations in 1 M KOH solution. (b) The corresponding linear fitting calibration curve for the determination of NH_4Cl, the inset is the optical images of the NH_4Cl standards stained with indophenol blue indicator. Error bars denote the standard deviations of absorbance from three independent tests.

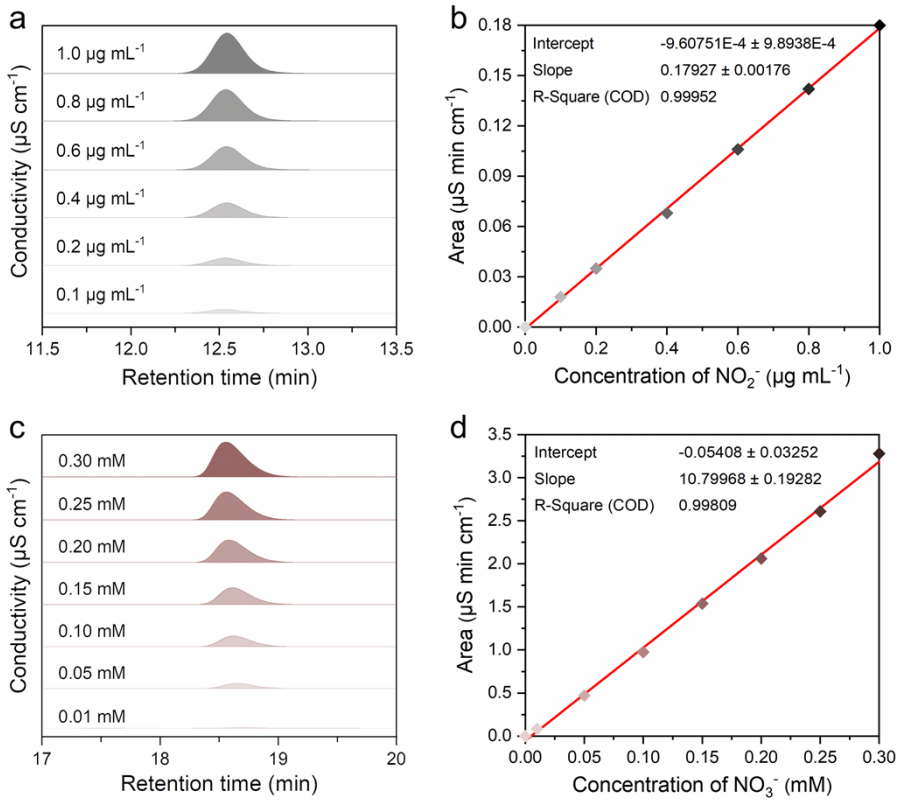

Figure S18. The ion chromatogram spectra for the standard NO_2^- (a), and the corresponding linear fitting calibration curves (b). The ion chromatogram spectra for the standard NO_3^- (c), and the corresponding linear fitting calibration curves (d).

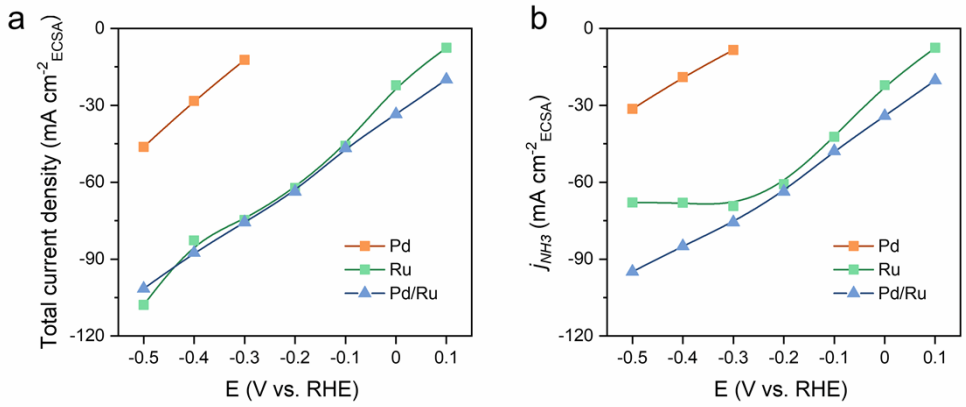

Figure S19. ECSA-normalized total current density (a) and NH_3 partial current density (j_{NH3}) (b) of Pd, Ru and $Pd_{74}Ru_{26}$.

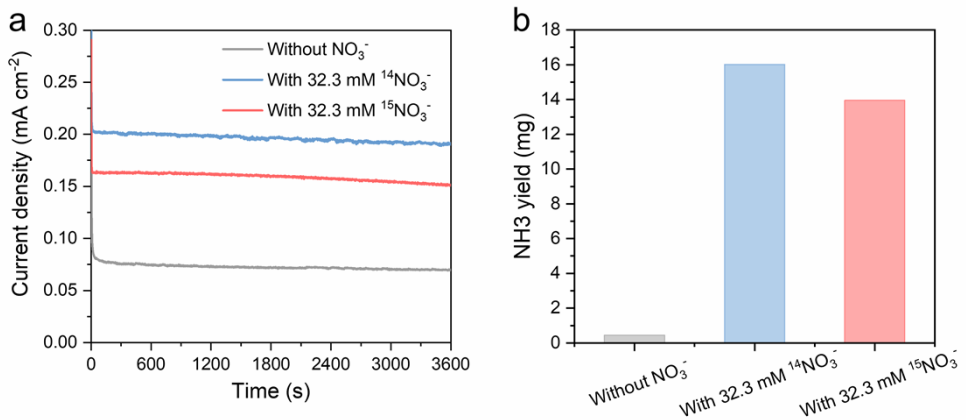

Figure S20. The i-t curves (a) of $Pd_{74}Ru_{26}$ at -0.3 V in 1 M KOH without NO_3^-, with 32.3 mM $^{14}NO_3^-$ and with 32.3 mM $^{15}NO_3^-$, respectively, and the corresponding NH_3 yields (b) in the post-reaction electrolyte.

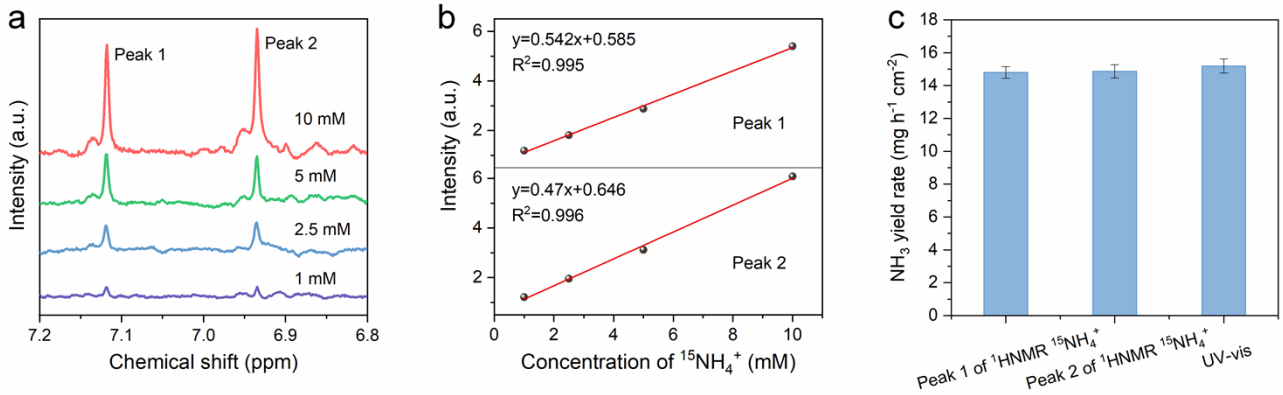

Figure S21. (a) ^{1}HNMR spectra of $^{15}NH_4^+$ with different concentrations. (b) The corresponding linear fitting calibration curve for $^{15}NH_4^+$ obtained from the intensity of two NMR peaks. (c) Comparison of the $^{15}NH_4^+$ yield rate quantified by the ^{1}H NMR and UV-vis spectra.

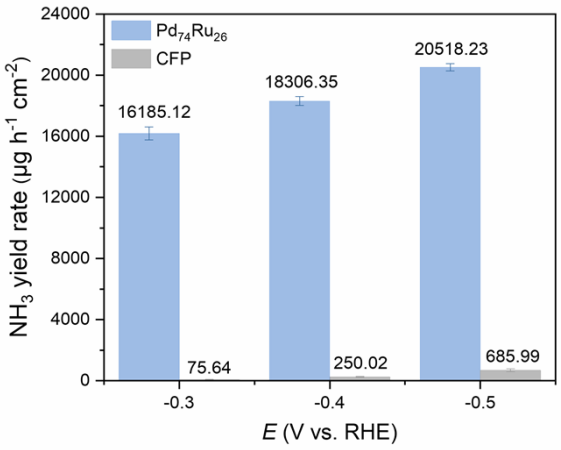

Figure S22. NH_3 yield rates of $Pd_{74}Ru_{26}$/CFP and bare CFP electrodes at different potentials in 1 M KOH with 32.3 mM NO_3^-.

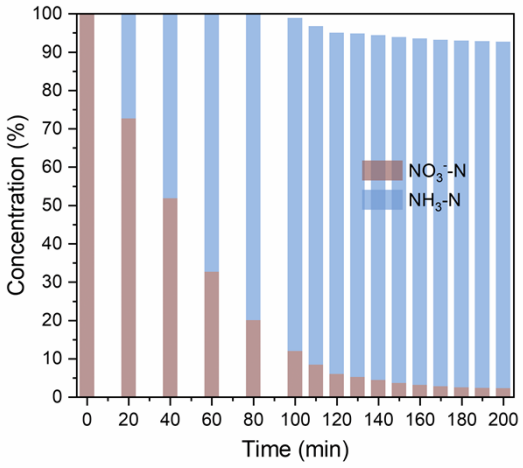

Figure S23. Time-dependent concentration ratios of NO_3^-–N, NH_3–N, and NO_2^-–N in the electrolyte during a continuous eNO_3^-RR at -0.3 V in a simulated industrial wastewater containing 1 M KOH and 32.3 mM NO_3^-.

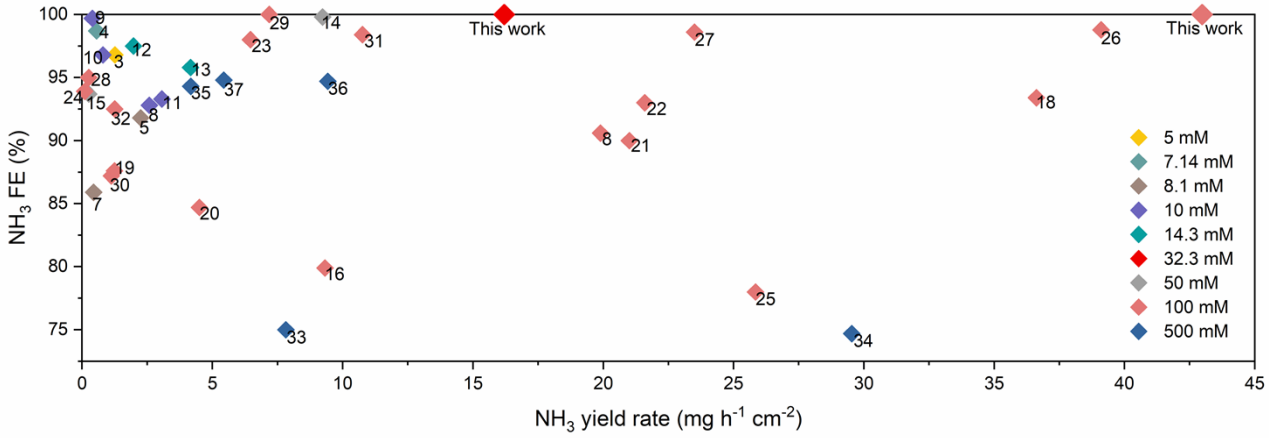

Figure S24. Comparison of NH_3 production performance of $Pd_{74}Ru_{26}$ NCs and other reported advanced eNO_3^-RR catalysts at different NO_3^- concentration, with references.

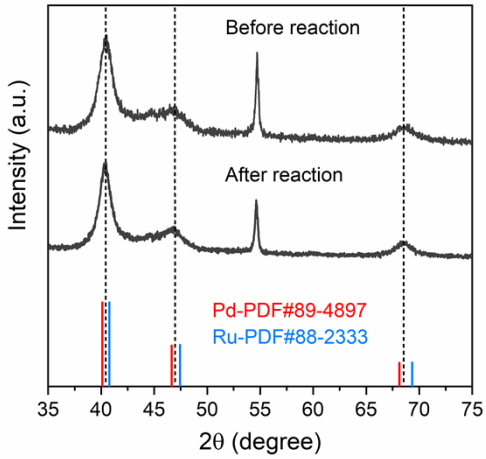

Figure S25. XRD patterns of $Pd_{74}Ru_{26}$ after the long-term chronopotentiometry (CP) test.

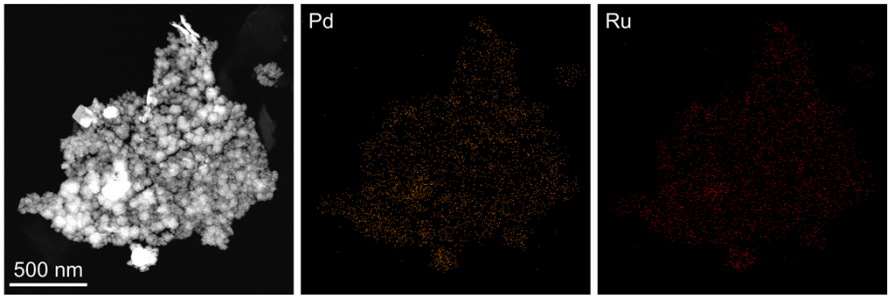

Figure S26. TEM mapping images of $Pd_{74}Ru_{26}$ after the long-term chronopotentiometry (CP) test.

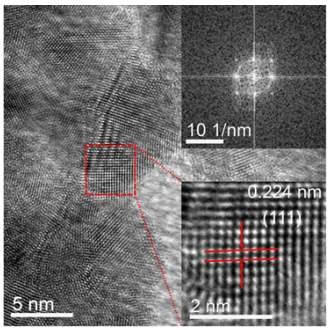

Figure S27. HRTEM image of $Pd_{74}Ru_{26}$ after the long-term chronopotentiometry (CP) test, and the corresponding FFT pattern (inset) of the selected area with the red dashed square.

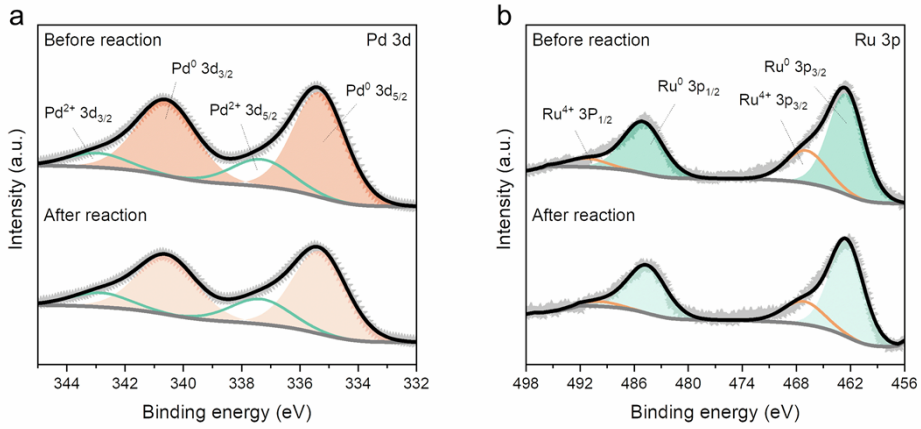

Figure S28. High-resolution Pd 3d XPS spectrum (a), and Ru 3p XPS spectrum (b) of $Pd_{74}Ru_{26}$ before/after the CP test.

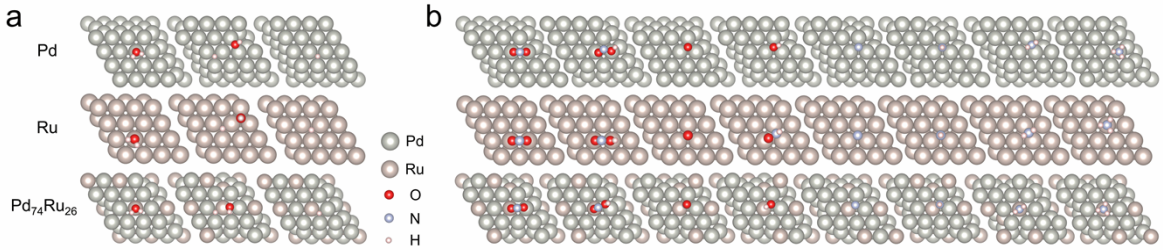

Figure S29. Optimized adsorption configurations of each intermediate on Pd(111), Ru(001) and $Pd_{74}Ru_{26}$(111) surfaces along the HER steps (a) and eNO_3RR steps (b) (top view).

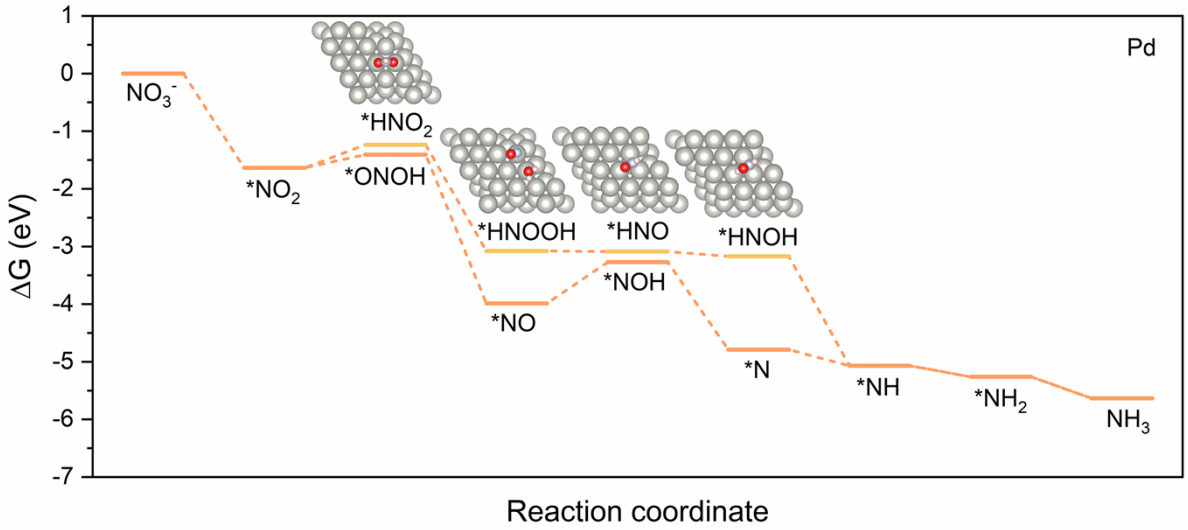

Figure S30. Free energy diagram of each intermediate state on Pd(111) surface along different eNO_3^- RR pathways calculated at 0 V vs. RHE.

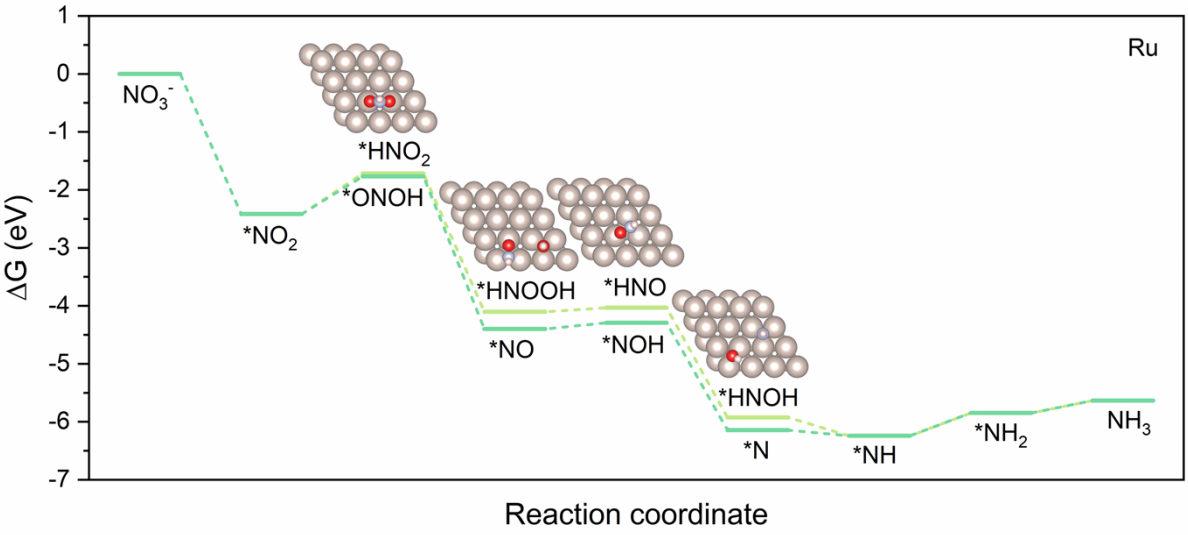

Figure S31. Free energy diagram of each intermediate state on Ru(001) surface along different eNO_3^- RR pathways calculated at 0 V vs. RHE.

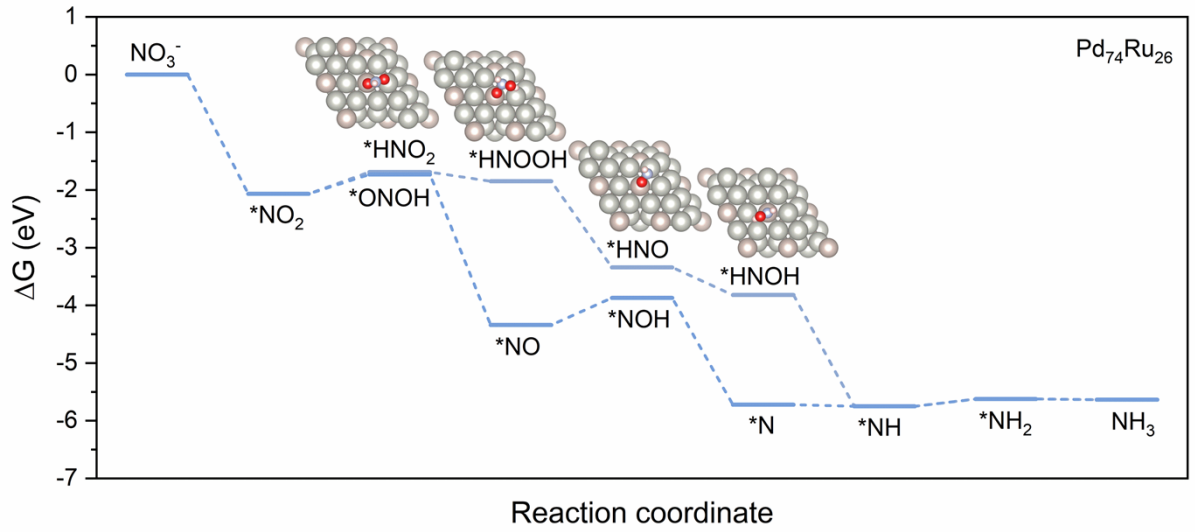

Figure S32. Free energy diagram of each intermediate state on $Pd_{74}Ru_{26}$(111) surface along different eNO_3^-RR pathways calculated at 0 V vs. RHE.

Table S1. Atomic ratios of Pd and Ru elements in Pd_xRu_y bimetallic NCs obtained by ICP-OES.

	$Pd_{90}Ru_{10}$	$Pd_{74}Ru_{26}$	$Pd_{57}Ru_{43}$
Pd: Ru atomic ratio	92.32: 7.68	69.44: 30.56	54.1: 45.9

Table S2. Surface metal elemental ratio calculated from XPS spectra of $Pd_{74}Ru_{26}$ NCs before and after reaction.

		Before reaction	**After reaction**
Pd (at%)	Pd^0	57.32	53.09
	Pd^{2+}	16.86	22.51
Ru (at%)	Ru^0	17.76	15.42
	Ru^{4+}	8.06	8.98

Table S3. Structural parameters of Pd foil, $Pd_{57}Ru_{43}$, $Pd_{74}Ru_{26}$, and $Pd_{90}Ru_{10}$ extracted from the EXAFS fitting. Multi (k^1, k^2, k^3)-weighted is carried out, the fitting range is $3 < k < 14$ Å^{-1}, $1 < R < 3$ Å, and $S_0^2 = 0.895$. S_0^2 represents the amplitude reduction factor, determined through the fitting of the Pd foil; CN is the coordination number; R is the interatomic distance (the bond length between Pd central atoms and surrounding coordination atoms); σ^2 is the Debye-Waller factor; ΔE_0 is edge energy shift; The R factor evaluates the quality of the fitting.

Sample	Scatter path	CN	R(Å)	σ^2 (Å^2)	ΔE_0(eV)
Pd foil	Pd-Pd	12	2.759±0.003	0.0056±0.0004	-3.7±0.6
$Pd_{57}Ru_{43}$	Pd-Pd/Ru	10.2±0.7	2.737±0.004	0.0071±0.0005	6.1±0.5
$Pd_{74}Ru_{26}$	Pd-Pd/Ru	10.5±0.8	2.744±0.004	0.0072±0.0005	7.6±0.5
$Pd_{90}Ru_{10}$	Pd-Pd/Ru	9.8±0.8	2.754±0.004	0.0068±0.0005	-5.1±0.6

Table S4. Estimated ECSAs of Pd, Ru and $Pd_{74}Ru_{26}$ NCs. The ECSA was determined by: ECSA = C_{dl}/C_s, where C_{dl} is the double layer capacitance and C_s is the specific capacitance of the sample. The specific capacitance for a flat surface is generally found to be in the range of 20-60 μF cm^{-2}. In this study, the specific capacitance is assumed to be Cs = 40 μF cm^{-2}.

	C_{dl} (μF cm^{-2})	**ECSA (cm^2)**
Pd	98.2	2.46
Ru	84.68	2.12
$Pd_{74}Ru_{26}$	110.08	2.75

Table S5. Comparison of performance of $Pd_{74}Ru_{26}$ NCs and other reported advanced electrocatalysts for NH_3 production via eNO_3^-RR.

Catalyst	**NO_3^- concentration (mM)**	**Applied potential (V vs. RHE)**	**NH_3 FE (%)**	**NH_3 yield rate (mg h^{-1} cm^{-2})**	**Ref.**
Ni_3Fe-CO_3 LDH	5	-0.2	96.8	1.261	[9]
Au_1Cu	7.14	-0.2	98.7	0.555	[10]
Fe@N-C	~8.1	-0.75	91.8	2.25	[11]
Pd-NDs/Zr-MOF	~8.1	-1.3	58.1	0.115	[12]
Cu–PTCDA	~8.1	-0.4	85.9	0.44	[13]
CuCoSP	10	-0.175	92.8	2.58	[14]
Cu-NSs	10	-0.15	99.7	0.39	[15]
Cu(B)-2	10	-0.7	96.8	0.798	[16]
CoP-CNS	10	-0.33	93.3	3.06	[17]
a-RuO_2	~14.3	-0.35	97.5	1.97	[18]
CuO NWAs	~14.3	-0.85	95.8	4.16	[19]
MP-Cu	50	-0.3	99.8	9.231	[20]

PA-RhCu cNCs	50	0.05	93.7	0.254	[21]
Pd Octohedron	100	-0.7	79.9	9.325	[22]
$Cu_{50}Ni_{50}$	100	~-0.15	99	–	[23]
CoO_x	100	-0.3	93.4	36.62	[24]
CuCoSP	100	-0.175	90.6	19.89	[14]
Fe_2TiO_5	100	-1.0	87.6	1.241	[25]
Cu-N_4 SAC	100	-1.0	84.7	4.50	[26]
Fe-cyano NSs	100	-0.5	90	21.00	[27]
Rh@Cu	100	-0.2	93	21.59	[28]
Ru_xCu_y/rGO	100	-0.05	98	6.46	[29]
FOSP-Cu	100	-0.266	93.9	0.101	[30]
Pd/NF	100	-1.4	78	25.84	[31]
Ru/β-$Co(OH)_2$	100	0.01	98.78	39.1	[32]
RuO_x/Pd	100	-0.5	98.6	23.5	[33]
Rh NFs	100	0.2	95	0.253	[34]
Cu-doped Fe_3O_4	100	-0.6	~100	7.18	[35]
ISAA In−Pd	100	-0.6	87.2%	1.122	[36]
Zn/Cu-2.3	100	-0.55	98.4	10.76	[37]
Fe/Cu-NG	100	-0.3	92.51	~1.25	[38]
Fe SACs	500	-0.66	75	7.82	[39]
Bi NCs	500	-0.8	74.7	29.53	[40]
Fe/Ni_2P	500	-0.4	94.3	4.17	[41]
NiO_4-CCP	500	-0.7	94.7	~9.43	[42]
ZnSA-MNC	500	-1.0	94.8	5.44	[43]
$Pd_{74}Ru_{26}$ NCs	**32.3** **100**	**-0.3** **-0.9**	**~100** **~100**	**16.20** **42.98**	**This work**

Reference

1. J.-Y. Fang, Q.-Z. Zheng, Y.-Y. Lou, K.-M. Zhao, S.-N. Hu, G. Li, O. Akdim, X.-Y. Huang and S.-G. Sun, Ampere-level current density ammonia electrochemical synthesis using CuCo nanosheets simulating nitrite reductase bifunctional nature, *Nat. Commun.*, 2022, **13**, 7899.

2. Y. Zhao, R. Shi, X. Bian, C. Zhou, Y. Zhao, S. Zhang, F. Wu, G. I. N. Waterhouse, L.-Z. Wu, C.-H. Tung and T. Zhang, Ammonia Detection Methods in Photocatalytic and Electrocatalytic Experiments: How to Improve the Reliability of NH_3 Production Rates?, *Adv. Sci*, 2019, **6**, 1802109.
3. G. Kresse and J. Furthmüller, Efficiency of ab-initio total energy calculations for metals and semiconductors using a plane-wave basis set, *Comput. Mater. Sci.*, 1996, **6**, 15-50.
4. G. Kresse and J. Furthmuller, Efficient iterative schemes for ab initio total-energy calculations using a plane-wave basis set, *Phys. Rev. B*, 1996, **54**, 11169-11186.
5. P. E. Blochl, Projector augmented-wave method, *Phys. Rev. B*, 1994, **50**, 17953-17979.
6. J. P. Perdew, K. Burke and M. Ernzerhof, Generalized gradient approximation made simple, *Phys. Rev. Lett.*, 1996, **77**, 3865-3868.
7. H. J. Monkhorst and J. D. Pack, Special points for Brillouin-zone integrations, *Phys. Rev. B*, 1976, **13**, 5188-5192.
8. J. K. Nørskov, J. Rossmeisl, A. Logadottir, L. Lindqvist, J. R. Kitchin, T. Bligaard and H. Jónsson, Origin of the overpotential for oxygen reduction at a fuel-cell cathode, *J. Phys. Chem. B*, 2004, **108**, 17886-17892.
9. K.-H. Kim, H. Lee, X. Huang, J. H. Choi, C. Chen, J. K. Kang and D. O'Hare, Energy-efficient electrochemical ammonia production from dilute nitrate solution, *Energy & Environmental Science*, 2023, **16**, 663-672.
10. Y. Zhang, X. Chen, W. Wang, L. Yin and J. C. Crittenden, Electrocatalytic nitrate reduction to ammonia on defective Au_1Cu (111) single-atom alloys, *Applied Catalysis B: Environmental*, 2022, **310**, 121346.
11. S. Zhang, M. Li, J. Li, Q. Song and X. Liu, N-doped carbon–iron heterointerfaces for boosted electrocatalytic active and selective ammonia production, *Proceedings of the National Academy of Sciences*, 2023, **120**, e2207080119.
12. M. Jiang, J. Su, X. Song, P. Zhang, M. Zhu, L. Qin, Z. Tie, J.-L. Zuo and Z. Jin, Interfacial Reduction Nucleation of Noble Metal Nanodots on Redox-Active Metal–Organic Frameworks for High-Efficiency Electrocatalytic Conversion of Nitrate to Ammonia, *Nano Letters*, 2022, **22**, 2529-2537.
13. G.-F. Chen, Y. Yuan, H. Jiang, S.-Y. Ren, L.-X. Ding, L. Ma, T. Wu, J. Lu and H. Wang, Electrochemical reduction of nitrate to ammonia via direct eight-electron transfer using a copper–molecular solid catalyst, *Nature Energy*, 2020, **5**, 605-613.
14. W. He, J. Zhang, S. Dieckhöfer, S. Varhade, A. C. Brix, A. Lielpetere, S. Seisel, J. R. C. Junqueira and

W. Schuhmann, Splicing the active phases of copper/cobalt-based catalysts achieves high-rate tandem electroreduction of nitrate to ammonia, *Nature Communications*, 2022, **13**, 1129.

15. X. Fu, X. Zhao, X. Hu, K. He, Y. Yu, T. Li, Q. Tu, X. Qian, Q. Yue, M. R. Wasielewski and Y. Kang, Alternative route for electrochemical ammonia synthesis by reduction of nitrate on copper nanosheets, *Applied Materials Today*, 2020, **19**, 100620.
16. L. Wu, L. Zhang, S. Liu, J. Feng, L. Xu, X. Tan, X. Ma and X. Sun, Promoting ambient ammonia electrosynthesis on modulated $Cu^{\delta+}$ catalysts by B-doping, *Journal of Materials Chemistry A*, 2023, **11**, 5520-5526.
17. K. Fan, W. Xie, J. Li, Y. Sun, P. Xu, Y. Tang, Z. Li and M. Shao, Active hydrogen boosts electrochemical nitrate reduction to ammonia, *Nature Communications*, 2022, **13**, 7958.
18. Y. Wang, H. Li, W. Zhou, X. Zhang, B. Zhang and Y. Yu, Structurally Disordered RuO_2 Nanosheets with Rich Oxygen Vacancies for Enhanced Nitrate Electroreduction to Ammonia, *Angewandte Chemie International Edition*, 2022, **61**, e202202604.
19. Y. Wang, W. Zhou, R. Jia, Y. Yu and B. Zhang, Unveiling the Activity Origin of a Copper-based Electrocatalyst for Selective Nitrate Reduction to Ammonia, *Angewandte Chemie International Edition*, 2020, **59**, 5350-5354.
20. W. Wen, P. Yan, W. Sun, Y. Zhou and X.-Y. Yu, Metastable Phase Cu with Optimized Local Electronic State for Efficient Electrocatalytic Production of Ammonia from Nitrate, *Advanced Functional Materials*, 2023, **33**, 2212236.
21. Z.-X. Ge, T.-J. Wang, Y. Ding, S.-B. Yin, F.-M. Li, P. Chen and Y. Chen, Interfacial Engineering Enhances the Electroactivity of Frame-Like Concave RhCu Bimetallic Nanocubes for Nitrate Reduction, *Advanced Energy Materials*, 2022, **12**, 2103916.
22. Y. Han, X. Zhang, W. Cai, H. Zhao, Y. Zhang, Y. Sun, Z. Hu, S. Li, J. Lai and L. Wang, Facet-controlled palladium nanocrystalline for enhanced nitrate reduction towards ammonia, *Journal of Colloid and Interface Science*, 2021, **600**, 620-628.
23. Y. Wang, A. Xu, Z. Wang, L. Huang, J. Li, F. Li, J. Wicks, M. Luo, D.-H. Nam, C.-S. Tan, Y. Ding, J. Wu, Y. Lum, C.-T. Dinh, D. Sinton, G. Zheng and E. H. Sargent, Enhanced Nitrate-to-Ammonia Activity on Copper–Nickel Alloys via Tuning of Intermediate Adsorption, *Journal of the American Chemical Society*, 2020, **142**, 5702-5708.
24. J. Wang, C. Cai, Y. Wang, X. Yang, D. Wu, Y. Zhu, M. Li, M. Gu and M. Shao, Electrocatalytic Reduction of Nitrate to Ammonia on Low-Cost Ultrathin CoO_x Nanosheets, *ACS Catalysis*, 2021, **11**,

15135-15140.

25. H. Du, H. Guo, K. Wang, X. Du, B. A. Beshiwork, S. Sun, Y. Luo, Q. Liu, T. Li and X. Sun, Durable Electrocatalytic Reduction of Nitrate to Ammonia over Defective Pseudobrookite Fe_2TiO_5 Nanofibers with Abundant Oxygen Vacancies, *Angewandte Chemie International Edition*, 2023, **62**, e202215782.
26. J. Yang, H. Qi, A. Li, X. Liu, X. Yang, S. Zhang, Q. Zhao, Q. Jiang, Y. Su, L. Zhang, J.-F. Li, Z.-Q. Tian, W. Liu, A. Wang and T. Zhang, Potential-Driven Restructuring of Cu Single Atoms to Nanoparticles for Boosting the Electrochemical Reduction of Nitrate to Ammonia, *Journal of the American Chemical Society*, 2022, **144**, 12062-12071.
27. Z. Fang, Z. Jin, S. Tang, P. Li, P. Wu and G. Yu, Porous Two-dimensional Iron-Cyano Nanosheets for High-rate Electrochemical Nitrate Reduction, *ACS Nano*, 2022, **16**, 1072-1081.
28. H. Liu, X. Lang, C. Zhu, J. Timoshenko, M. Rüscher, L. Bai, N. Guijarro, H. Yin, Y. Peng, J. Li, Z. Liu, W. Wang, B. R. Cuenya and J. Luo, Efficient Electrochemical Nitrate Reduction to Ammonia with Copper-Supported Rhodium Cluster and Single-Atom Catalysts, *Angewandte Chemie International Edition*, 2022, **61**, e202202556.
29. W. Gao, K. Xie, J. Xie, X. Wang, H. Zhang, S. Chen, H. Wang, Z. Li and C. Li, Alloying of Cu with Ru Enabling the Relay Catalysis for Reduction of Nitrate to Ammonia, *Advanced Materials*, 2023, **35**, 2202952.
30. Y. Zhao, Y. Liu, Z. Zhang, Z. Mo, C. Wang and S. Gao, Flower-like open-structured polycrystalline copper with synergistic multi-crystal plane for efficient electrocatalytic reduction of nitrate to ammonia, *Nano Energy*, 2022, **97**, 107124.
31. H. Guo, M. Li, Y. Yang, R. Luo, W. Liu, F. Zhang, C. Tang, G. Yang and Y. Zhou, Self-Supported Pd Nanorod Arrays for High-Efficient Nitrate Electroreduction to Ammonia, *Small*, 2023, **19**, 2207743.
32. W. Zhu, F. Yao, Q. Wu, Q. Jiang, J. Wang, Z. Wang and H. Liang, Weakened d–p orbital hybridization in in situ reconstructed Ru/β-$Co(OH)_2$ heterointerfaces for accelerated ammonia electrosynthesis from nitrates, *Energy & Environmental Science*, 2023, **16**, 2483-2493.
33. X. Li, P. Shen, X. Li, D. Ma and K. Chu, Sub-nm RuO_x Clusters on Pd Metallene for Synergistically Enhanced Nitrate Electroreduction to Ammonia, *ACS Nano*, 2023, **17**, 1081-1090.
34. H. Liu, J. Timoshenko, L. Bai, Q. Li, M. Rüscher, C. Sun, B. Roldan Cuenya and J. Luo, Low-Coordination Rhodium Catalysts for an Efficient Electrochemical Nitrate Reduction to Ammonia, *ACS Catalysis*, 2023, **13**, 1513-1521.
35. J. Wang, Y. Wang, C. Cai, Y. Liu, D. Wu, M. Wang, M. Li, X. Wei, M. Shao and M. Gu, Cu-Doped

Iron Oxide for the Efficient Electrocatalytic Nitrate Reduction Reaction, *Nano Letters*, 2023, **23**, 1897-1903.

36. M. Xie, S. Tang, Z. Li, M. Wang, Z. Jin, P. Li, X. Zhan, H. Zhou and G. Yu, Intermetallic Single-Atom Alloy In–Pd Bimetallene for Neutral Electrosynthesis of Ammonia from Nitrate, *Journal of the American Chemical Society*, 2023, **145**, 13957-13967.
37. L. Wu, J. Feng, L. Zhang, S. Jia, X. Song, Q. Zhu, X. Kang, X. Xing, X. Sun and B. Han, Boosting Electrocatalytic Nitrate-to-Ammonia via Tuning of N-Intermediate Adsorption on a Zn−Cu Catalyst, *Angewandte Chemie International Edition*, 2023, **n/a**, e202307952.
38. S. Zhang, J. Wu, M. Zheng, X. Jin, Z. Shen, Z. Li, Y. Wang, Q. Wang, X. Wang, H. Wei, J. Zhang, P. Wang, S. Zhang, L. Yu, L. Dong, Q. Zhu, H. Zhang and J. Lu, Fe/Cu diatomic catalysts for electrochemical nitrate reduction to ammonia, *Nature Communications*, 2023, **14**, 3634.
39. Z.-Y. Wu, M. Karamad, X. Yong, Q. Huang, D. A. Cullen, P. Zhu, C. Xia, Q. Xiao, M. Shakouri, F.-Y. Chen, J. Y. Kim, Y. Xia, K. Heck, Y. Hu, M. S. Wong, Q. Li, I. Gates, S. Siahrostami and H. Wang, Electrochemical ammonia synthesis via nitrate reduction on Fe single atom catalyst, *Nature Communications*, 2021, **12**, 2870.
40. N. Zhang, J. Shang, X. Deng, L. Cai, R. Long, Y. Xiong and Y. Chai, Governing Interlayer Strain in Bismuth Nanocrystals for Efficient Ammonia Electrosynthesis from Nitrate Reduction, *ACS Nano*, 2022, **16**, 4795-4804.
41. R. Zhang, Y. Guo, S. Zhang, D. Chen, Y. Zhao, Z. Huang, L. Ma, P. Li, Q. Yang, G. Liang and C. Zhi, Efficient Ammonia Electrosynthesis and Energy Conversion through a Zn-Nitrate Battery by Iron Doping Engineered Nickel Phosphide Catalyst, *Advanced Energy Materials*, 2022, **12**, 2103872.
42. Y. Zhang, H. Zheng, K. Zhou, J. Ye, K. Chu, Z. Zhou, L. Zhang and T. Liu, Conjugated Coordination Polymer as a New Platform for Efficient and Selective Electroreduction of Nitrate into Ammonia, *Advanced Materials*, 2023, **35**, 2209855.
43. J. Zhao, X. Ren, X. Liu, X. Kuang, H. Wang, C. Zhang, Q. Wei and D. Wu, Zn single atom on N-doped carbon: Highly active and selective catalyst for electrochemical reduction of nitrate to ammonia, *Chemical Engineering Journal*, 2023, **452**, 139533.